



Three-dimensional mineral prospectivity mapping using a residual convolutional neural network with lightweight attention mechanisms[☆]

Zhiqiang Zhang^{a,b,c}, Gongwen Wang^{d,e,*}, Emmanuel John M. Carranza^f, Wei Li^{d,e}, Yingjie Li^{a,b,c}, Li Tang^e, Xinxing Liu^{a,b,c}

^a Hebei Province Collaborative Innovation Center for Strategic Critical Mineral Research, Hebei GEO University, Shijiazhuang 050031, PR China

^b Hebei Key Laboratory of Strategic Critical Mineral Resources, Hebei GEO University, Shijiazhuang 050031, PR China

^c School of Earth Sciences, Hebei GEO University, Shijiazhuang 050031, PR China

^d MNR Key Laboratory for Exploration Theory & Technology of Critical Mineral Resources, China University of Geosciences, Beijing 100083, PR China

^e School of Earth Sciences and Resources, China University of Geosciences, Beijing 100083, PR China

^f Geological of Geology, Faculty of Natural and Agricultural Sciences, University of the Free State, Bloemfontein, South Africa

ARTICLE INFO

Keywords:

Three-dimensional residual convolutional neural network

Lightweight attention mechanisms

Three-dimensional mineral prospectivity mapping

Wulong gold district

ABSTRACT

The continuous exploration and mining of surface and shallow mineral resources have promoted subsurface exploration. Over the past decade, mineral prospectivity mapping (MPM) has progressively expanded from two-dimensional (2D) to three-dimensional (3D). The 3D convolutional neural networks (CNN) and attention mechanisms (AMs) are adept at processing 3D voxel data, offering significant advantages for 3D MPM. However, the larger computational cost in a 3D CNN-AMs model presents limitations, constraining its application to 3D MPM. This study presents a new 3D CNN architecture composed of residual blocks (ResBlocks) and a lightweight Attention Mechanism (LAM) for 3D MPM. ResBlocks incorporate skip connections to deepen the network structure, thereby enhancing its ability to model complex nonlinear patterns and mitigating the vanishing gradient problem. The LAM utilizes the dimensionality reduction fully connected layer for channel attention and depthwise separable convolution for spatial attention, thus reducing computational costs. A case study in the Wulong gold district demonstrates that the proposed architecture achieves performance improvements in 3D MPM without significant increases in numbers of parameter count and FLOPs, highlighting its efficiency and effectiveness. Furthermore, the 3D mineral targets obtained in this study are beneficial for subsurface gold exploration in the Wulong Au district, China.

1. Introduction

Mineral prospectivity mapping (MPM) is a technique based on geographic information system (GIS) that uses geoscience datasets to systematically identify high potential areas for mineral exploration (Carranza et al., 2008). Given the extensive history of mining across the globe, the majority of surface and shallow deposits have already been discovered and mined (Manzi et al., 2015). Consequently, since 2010, the focus on MPM has progressively expanded from surface two-dimensional (2D) to subsurface three-dimensional (3D) (Wang et al., 2021). To the best of our knowledge, 3D MPM is predominantly conducted in brownfields due to its reliance on multi-scale 3D geological

models (e.g., 3D deposit and district scale models) (Wang et al., 2021). These 3D geological models are constructed mainly using geological and geophysical datasets, including geological maps, cross-section maps, boreholes, petrophysical, potential field, and magnetotelluric (MT) data (Olierook et al., 2021; Wu et al., 2024). With the development of explicit and implicit 3D geological modeling methodologies, current modeling approaches can enhance the accuracy and rationality of models by integrating geological and geophysical inversion data, along with incorporating expert knowledge (Lyu et al., 2021; Olierook et al., 2021). Deriving evidence layers associated with mineralization from 3D geological model constitutes the critical step in 3D MPM. Recently, various techniques of spatial analysis, such as 3D buffering (Tao et al.,

[☆] This article is part of a special issue entitled: 'Cu-Au in Middle-East China' published in Ore Geology Reviews.

* Corresponding author at: MNR Key Laboratory for Exploration Theory & Technology of Critical Mineral Resources, China University of Geosciences, Beijing 100083, PR China.

E-mail address: gwwang@cugb.edu.cn (G. Wang).

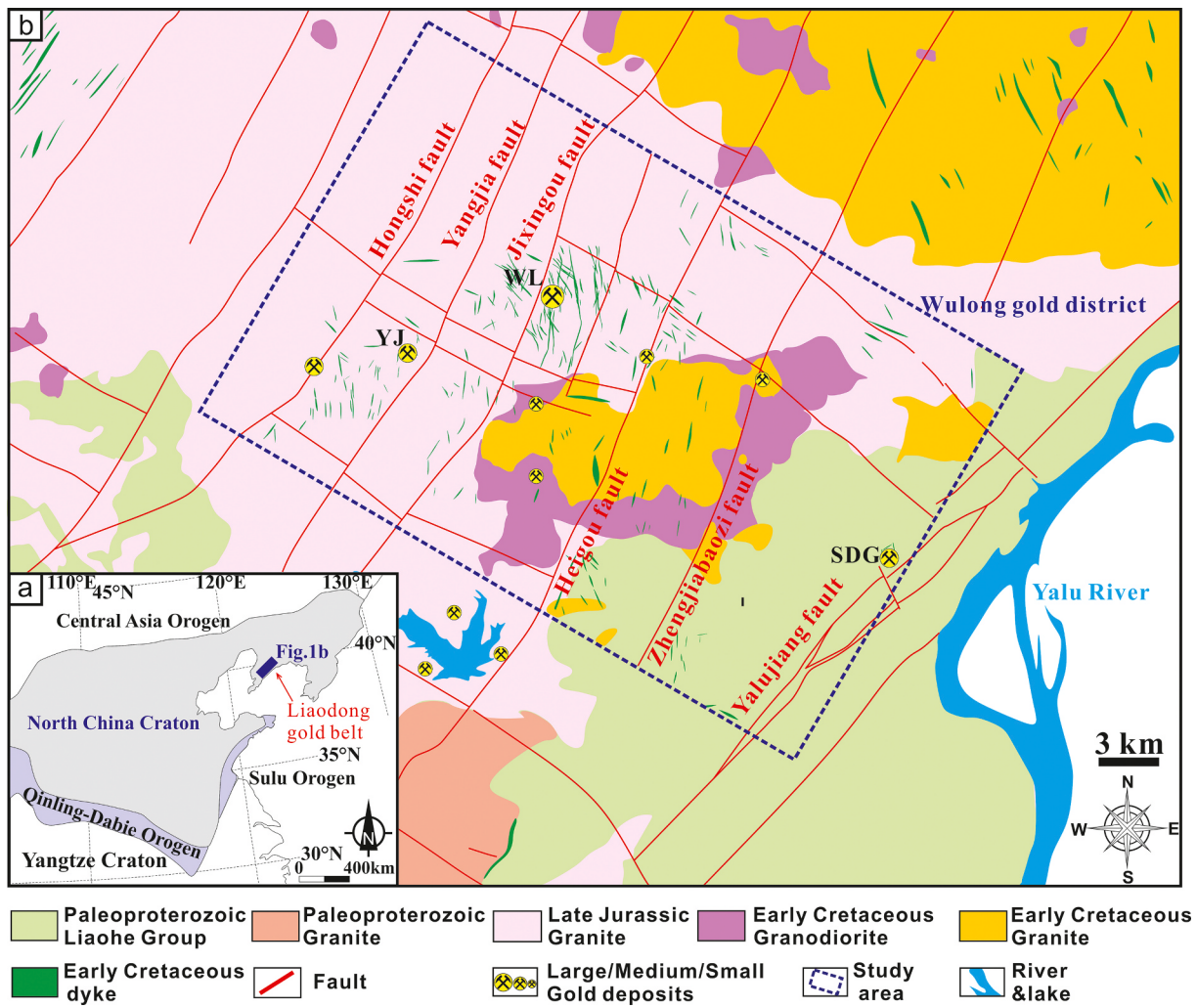


Fig. 1. (a) Location of the Liaodong gold belt. (b) Geological map of the study area.

2021), fractal analysis (Xiao et al., 2021), and morphological analysis (Deng et al., 2022), for extracting MPM evidence layers from 3D geological models have considerably enhanced the capacity of evidence layers to precisely outline exploration targets.

Data-driven methodologies, which are critical in integrating evidence layers for MPM in brownfields (Carranza et al., 2008; Zuo, 2020), are generally classified into three main categories (Zuo, 2020): statistics-based, shallow machine learning (ML)-based, and deep learning (DL)-based approaches. The weight-of-evidence and its advanced variants are typical methods of statistics-based data-driven approaches (Carranza et al., 2008). Since 2010, a variety of shallow ML algorithms, including support vector machines (SVM) (Zuo and Carranza, 2011), restricted Boltzmann machines (RBM) (Chen, 2015), and random forests (RF) (Zhang et al., 2022), have been employed in MPM to great effect. These shallow ML algorithms provide substantial benefits in integrating nonlinear and complex multivariate evidence layers for MPM (Zuo, 2020). Relative to statistics-based and shallow ML-based data-driven methodologies (Xiong et al., 2018; Li et al., 2021a), DL algorithms offer two critical advantages for MPM: (1) extraction of high-level informative features – DL algorithms excel in automatic extraction of high-level informative features from evidence layers (Zuo, 2020); and (2) capturing spatial patterns – DL extends beyond analysis of data within a single voxel, taking into account the relationships among neighboring voxels, which enables a more comprehensive analysis of the spatial features of mineralization (Li et al., 2023). Recently, DL algorithms, such as convolutional neural networks (CNN) (Li et al., 2020a), recurrent

neural networks (RNN) (Yin et al., 2022), graph neural networks (GNN) (Shi et al., 2024), and attention mechanisms model (AMs) (Deng et al., 2022) were utilized in MPM. Traditional DL algorithms typically treat all evidence layers uniformly (Yin et al., 2023; Xu and Zuo, 2024). In contrast, AMs enable these models to prioritize and focus on the more significant portions of individual evidence layers, thereby enhancing their feature representation capabilities (Woo et al., 2018; Wang and Zuo, 2022). Compared with traditional CNNs, a CNN that incorporates AMs (i.e., a CNN-AMs model) can dynamically refine the features produced by the convolutional layers. This adjustment allows the model to focus more intensively on information that is critical for effective MPM. In 2D MPM, the CNN-AMs model has demonstrated exceptional effectiveness (Yin et al., 2023). For 3D MPM, previous studies transformed fault-related evidence layers into 2D multi-channel images (Deng et al., 2022). Subsequently, the convolutional block attention module (CBAM), which encompasses both spatial and channel AMs was integrated into 2D CNN for structure-controlled gold prospectivity modeling (Liu et al., 2023). Compared to the 2D CNN-AMs model, the 3D CNN-AMs model is inherently more suited for 3D MPM because it can process 3D voxel data (Li et al., 2023). However, the larger computational cost incurred by a 3D CNN-AMs model presents limitations, constraining its application to 3D MPM. Zhang et al. (2023b) focused on developing lightweight CNN models tailored for 3D MPM. However, limited studies focused on lightweight 3D CNN-AMs model for 3D MPM.

The Wulong gold district is the largest gold district on the Liaodong gold belt (Fig. 1a) (Feng et al., 2023; Zhu et al., 2024). In this study, we

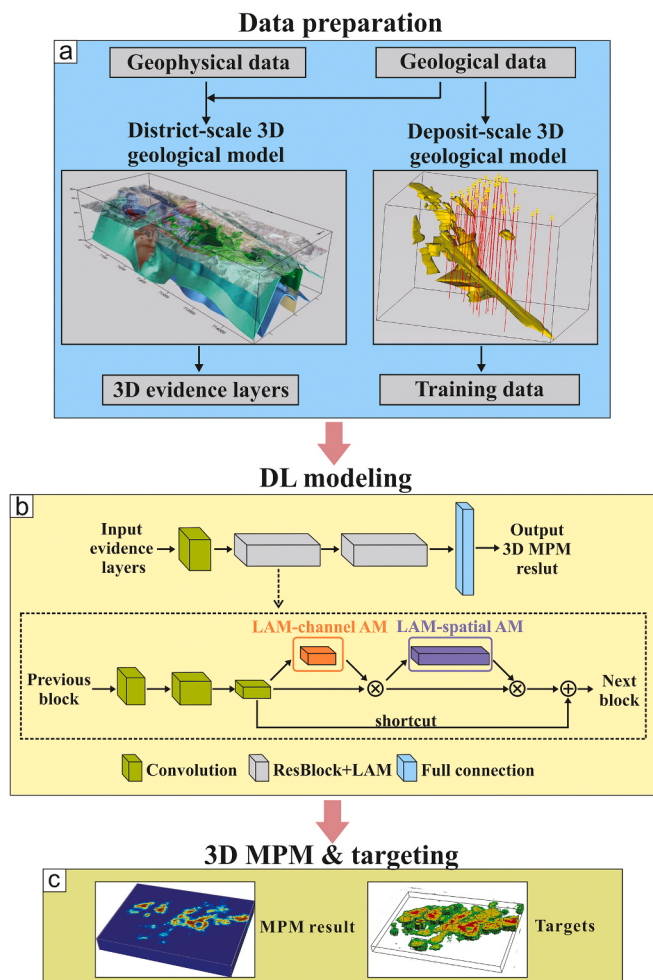


Fig. 2. Detailed workflow of this study (a) Multi-scale geophysical and geological datasets were used to construct district-scale and deposit-scale 3D geological models, providing 3D evidence layers and training data. (b) Architecture of the DL model. (c) 3D MPM and targeting.

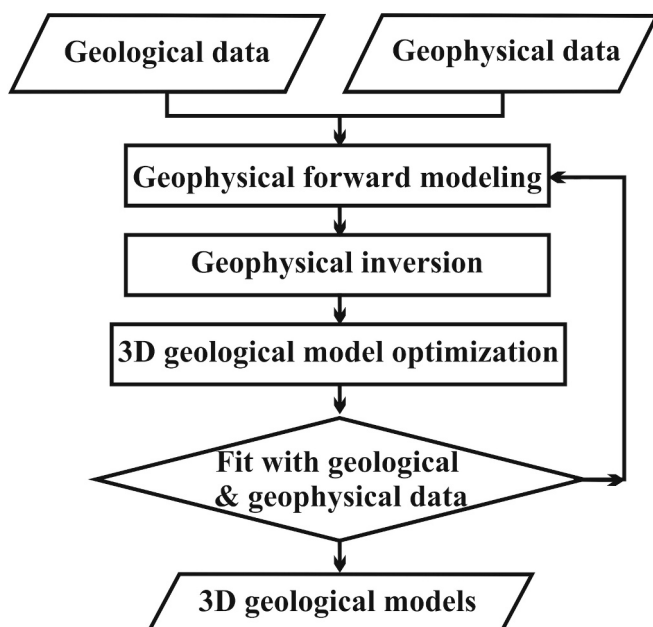


Fig. 3. Workflow of 3D geological modeling.

first constructed a 3D district-scale and deposit-scale geological model (Fig. 2a). Then, a novel 3D CNN architecture consisting of residual blocks (ResBlocks) and a lightweight attention module (LAM) was proposed for 3D MPM (Fig. 2b). The architecture is divided into two core components: (1) the ResBlocks, which integrate skip connections to facilitate direct information flow across layers, significantly mitigates the computational demands of 3D CNN; this component not only addresses the pervasive issue of vanishing gradients in deep networks but it also enhances substantially the network's capacity to learn complex representations; and (2) the LAM, engineered for efficiency, utilizes the dimensionality reduction fully connected layer for channel attention and the depthwise separable convolution for spatial attention, effectively reducing the model's computational cost. Finally, a subsurface targeting map to a depth of 5000 m in the study area has been mapped to support decision-making for exploration (Fig. 2c). The case study conducted in the Wulong gold district proved the efficiency and effectiveness of our proposed DL architecture for 3D MPM.

2. Geological overview

The Wulong gold district is situated on the Liaodong gold belt (Fig. 1a) (Zhu et al., 2024). There are extensive outcropped Mesozoic intrusions, including the Late Jurassic granite (164–155 Ma), the Early Cretaceous granodiorite (132–126 Ma), and Early Cretaceous dykes (predominantly composed of diorite and lamprophyre) (127–112 Ma) (Yu et al., 2018). The exposed strata belong to the Paleoproterozoic Liaohe Group (Fig. 1b) (Du et al., 2023). Additionally, Paleoproterozoic granites, which constitute the bedrock, outcrop on the southeastern periphery of the study area (Fig. 1b). The orebodies in the study area exhibit an emplacement mechanism that closely mirrors that of the Early Cretaceous dikes, with which they have significant spatial associations (Zhu et al., 2024). The dating of minerals associated with gold, including molybdenite and pyrite (using Rb-Sr), hydrothermal monazite (using U-Th-Pb), and sericite (using Ar-Ar), established the age of gold mineralization within the district during 125–115 Ma (Feng et al., 2019, 2023). This timeframe closely aligns with the period of the Early Cretaceous intrusions, indicating a temporal connection between the gold mineralization and the magmatic activity during Early Cretaceous. Isotope data—including S, Pb, He, Ar in pyrite, H and O in quartz—suggest that the ore-forming fluids predominantly originated from magmatic sources (Du et al., 2023). The study area is traversed by subparallel NE–NNE-striking faults (Fig. 1b). Additionally, a series of concealed NW-striking faults were identified through geophysical investigations (Zheng et al., 2022).

The gold deposits within the study area predominantly consist of the large vein-type Wulong gold deposit (WL), the medium vein-type Yangjia gold deposit (YJ), and the medium disseminated Sidaogou gold deposit (SDG) (Du et al., 2023). With the exception of the SDG, all other known gold deposits in the study area are located within Mesozoic intrusions (Fig. 1b). The spatial arrangement of these deposits and their orebodies is principally governed by NE–NNE-striking faults (Pang et al., 2018). However, some orebodies, such as the V163 orebody of WL, are also situated along NW-striking faults (Pang et al., 2022).

In summary, previous studies have demonstrated that the study area under investigation contains an intrusion-related gold mineral system (IRGS) closely connected with Early Cretaceous intrusions (Zhu et al., 2024). The ore-forming fluids, originating from these intrusions, traveled along faults, resulting in mineralization within favorable traps situated along these faults (Zhang et al., 2019).

3. 3D geological modeling and evidence layers

The 3D geological models were constructed via the SKUA–GoCAD software via geological and geophysical data. The detailed workflow was shown in Fig. 3. The 1:5000 scale district geological map, profiles, ground gravity, magnetic, and MT data were utilized to construct the

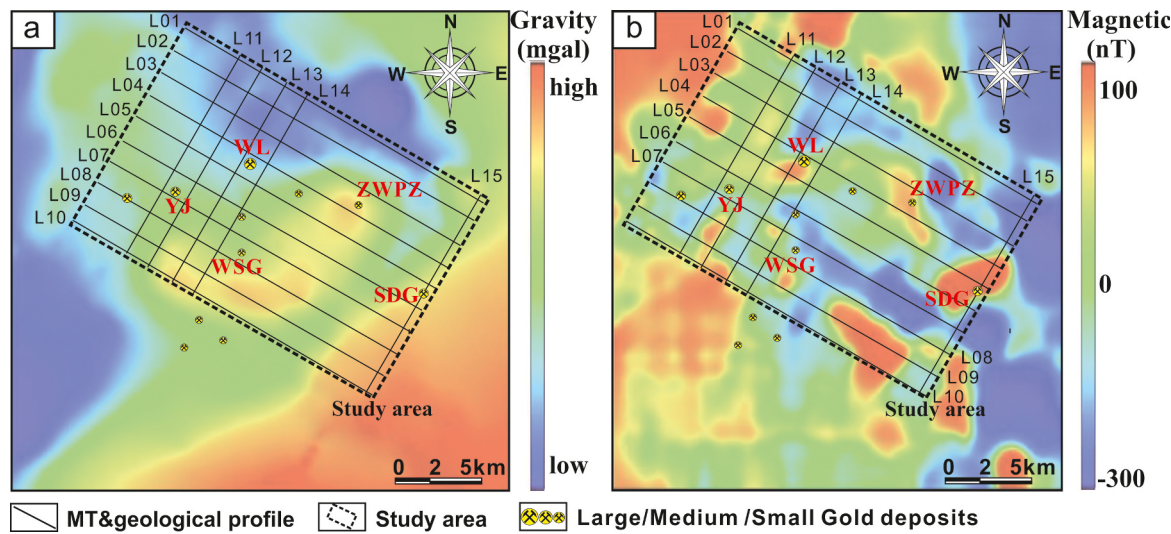


Fig. 4. (a) Residual gravity and (b) magnetic anomaly maps.

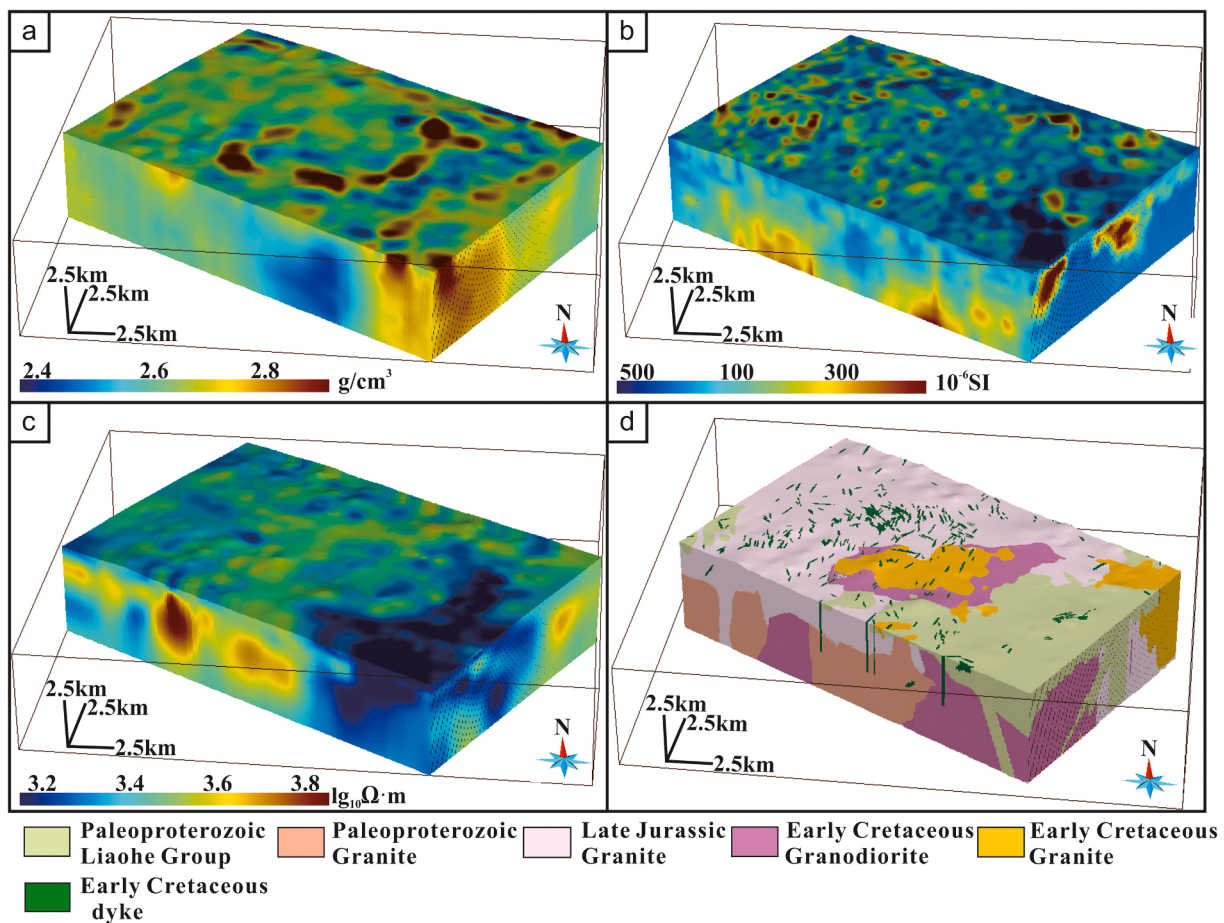


Fig. 5. (a) Gravity. (b) magnetic. (c) MT inversion models and (d) district-scale geological model.

district-scale 3D geological model. The modeling process and data of study area for the district-scale 3D geological model and orebody models were detail introduced in Zhang et al. (2019). To account for computational limitations and the smallest identifiable geological body, the 3D geological models were assigned a cell size of $50 \times 50 \times 50$ m, which is sufficient for district-scale exploration. The residual gravity (Fig. 4a) and magnetic (Fig. 4b) anomaly data, which utilized for 3D potential field

forward modeling and inversions, were obtained by empirical mode decomposition (Zhang et al., 2019). The potential field inversions were conducted via the UBC-GIF software. The MT inversion was conducted via Winglink software by the China Geological Survey. Both inversion types used a mesh size matching the cell size of 3D geological model ($50 \times 50 \times 50$ m), with results displayed in Fig. 5a, b and c, respectively. Fig. 5d displays the district-scale 3D geological model. The Early

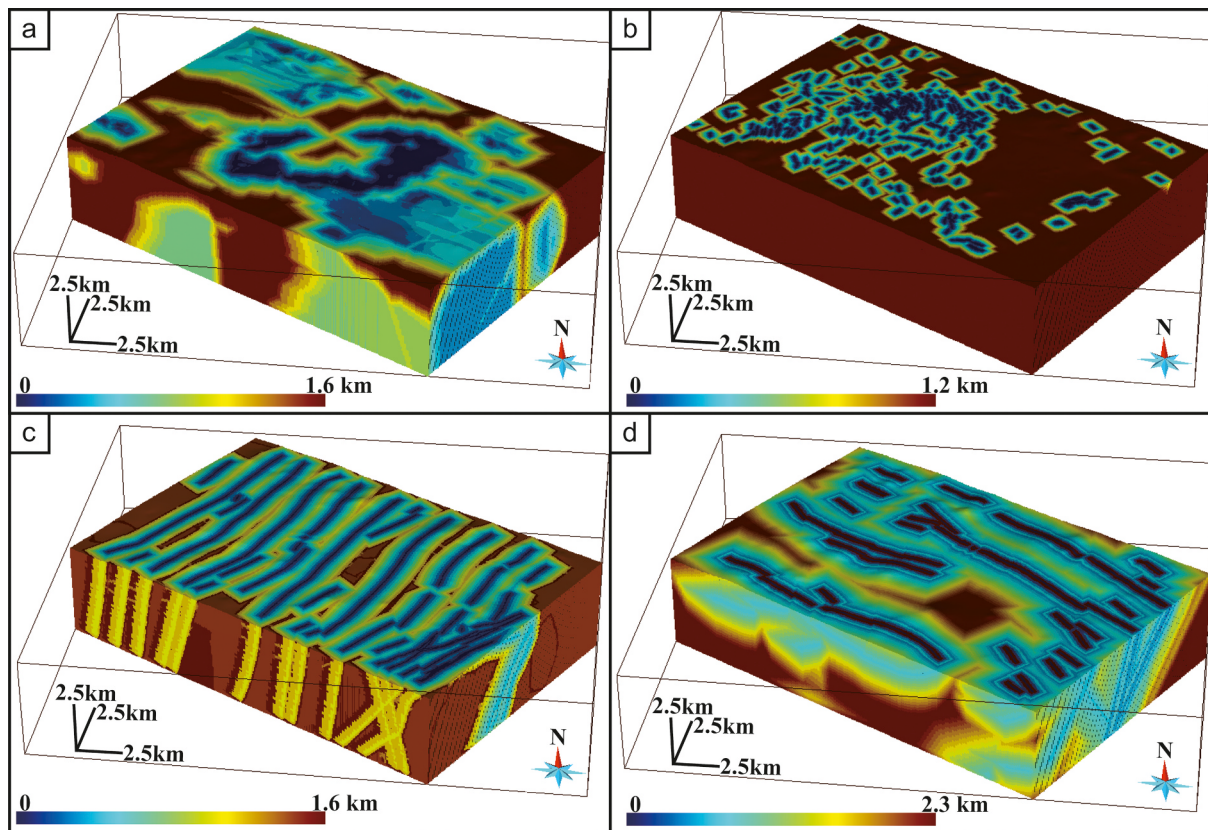


Fig. 6. 3D evidence layers models: (a) Early Cretaceous granodiorite. (b) Early Cretaceous dyke. (c) NE–NNE-striking faults and (d) NW-striking faults.

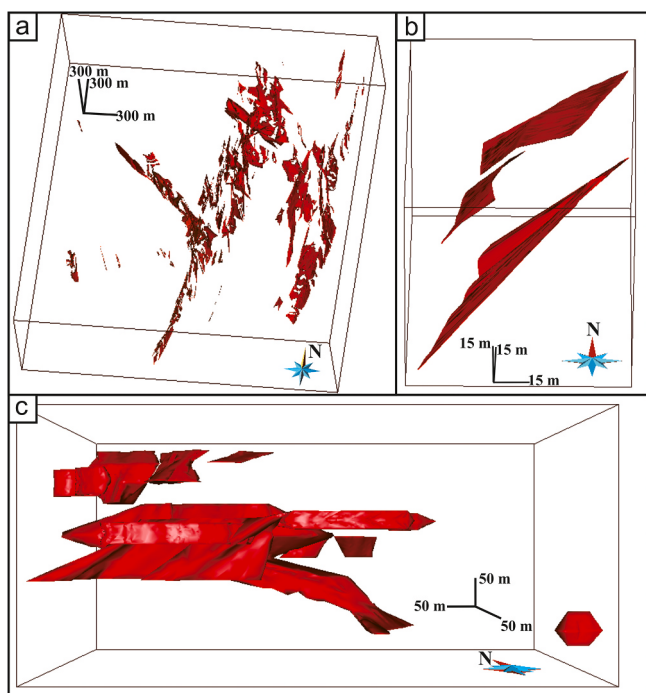


Fig. 7. 3D orebody models of the (a) WL, (b) YJ, and (c) SDG.

Cretaceous granodiorite and dyke models serve as sources of heat and fluids. The NE–NNE- and NW-striking faults models were considered spatial proxies of pathways and traps for mineralization. These 3D models were transformed into evidence layers via 3D buffer analysis (Fig. 6). The geophysical evidence layers were achieved through

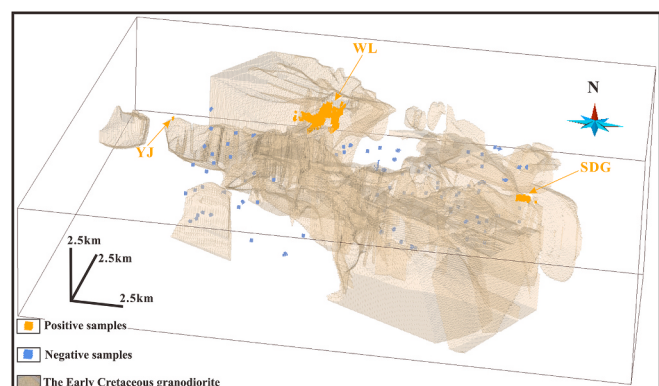


Fig. 8. Distribution of 2.5% randomly selected positive and negative samples in the study area.

Table 1
Accuracy, AUC, F1-score, NP, and FLOPs of DL and RF models.

Model	Accuracy	AUC	F1 score	NP	FLOPs
RF	0.865	0.924	0.823	58,905	58,905
DL1 (1conv + 1Resblock)	0.921	0.943	0.861	242,178	4,307,584
DL2 (1conv + 2Resblock)	0.941	0.965	0.889	480,130	8,583,808
DL3 (1conv + 1Resblock_LAM)	0.935	0.958	0.881	270,410	4,479,872
DL4 (1conv + 2Resblock_LAM)	0.962	0.981	0.917	536,594	8,928,384

Table 2
Hyperparameters of the DL4 model.

Layer name	Input channels	Kernel size	Stride	Padding	Out channels
Convolution	7	(3, 3, 3)	(1, 1, 1)	(1, 1, 1)	64
ResBlock1					
– Convolution 1	64	(3, 3, 3)	(1, 1, 1)	(1, 1, 1)	128
– Convolution 2	128	(3, 3, 3)	(1, 1, 1)	(1, 1, 1)	128
– Convolution 3 (shortcut)	128	(1, 1, 1)	(1, 1, 1)	(0, 0, 0)	128
– LAM-Channel AM-fully connected layer 1	128	—	—	—	8
– LAM-Channel AM-fully connected layer 2	8	—	—	—	128
– LAM-Spatial AM-depthwise separable convolution	128	(3, 3, 3)	(1, 1, 1)	(1, 1, 1)	128
– LAM-Spatial AM-pointwise convolution	128	(1, 1, 1)	(1, 1, 1)	(0, 0, 0)	64
ResBlock2					
– Convolution 1	64	(3, 3, 3)	(1, 1, 1)	(1, 1, 1)	128
– Convolution layer 2	128	(3, 3, 3)	(1, 1, 1)	(1, 1, 1)	128
– Convolution 3 (shortcut)	128	(1, 1, 1)	(1, 1, 1)	(0, 0, 0)	128
– LAM-Channel AM-fully connected layer 1	128	—	—	—	8
– LAM-Channel AM-fully connected layer 2	8	—	—	—	128
– LAM-Spatial AM-depthwise separable convolution	128	(3, 3, 3)	(1, 1, 1)	(1, 1, 1)	128
– LAM-Spatial AM-pointwise convolution	128	(1, 1, 1)	(1, 1, 1)	(0, 0, 0)	64
Full connection	64	—	—	—	2

geophysical inversions. The 1:500 scale deposit geological profile, 1:100 scale mine plans, and 45 boreholes were utilized to construct the 3D orebody models. Fig. 7 presents the 3D orebody models for WL, YJ, and SDG, employed as positive training samples.

4. Methodologies

4.1. Convolution neural network (CNN)

A standard CNN architecture is distinguished by three core parts: the convolutional layers, the pooling layers, and the fully connected layers (Alzubaidi et al., 2021). In this architectural paradigm, convolutional layers are responsible for extracting high-level spatial features from original data (Krizhevsky et al., 2012). Subsequently, pooling layers decrease the number of parameters and computational complexity by reducing data's dimensionality (Gholamalinezhad and Khosravi, 2020). Finally, the fully connected layers synthesize the extracted features to execute specific tasks, such as classification or regression (Ramachandran et al., 2017). Activation functions play a critical role in CNN modeling, introducing non-linearity that allows a model to capture and represent complex patterns (Ramachandran et al., 2017). The rectified linear unit (ReLU) function is a typical non-linearity activation

function, which can also address the vanishing and exploding gradient issues in DL (Glorot et al., 2011). Furthermore, the sigmoid function can transform the raw binary-classified output of a network into output as probabilities (Han and Moraga, 1995). The efficacy of a CNN is evaluated through a loss function (Krizhevsky et al., 2012). Through the process of back-propagation, the CNN adjusts its parameters using gradient descent, aiming to minimize the loss function (Rumelhart et al., 1986).

4.2. Residual blocks (ResBlocks)

A typical CNN comprises multiple hidden layers. Generally, adding more hidden layers enhances the performance of a CNN, indicating that a deeper network is usually more effective (Krizhevsky et al., 2012). The learning process of a CNN is from lower to higher layers. A feature map generated by a traditional two-layer CNN can be represented as:

$$\mathbf{Y} = \text{ReLU}(\mathbf{W}_2 * \text{ReLU}(\mathbf{W}_1 * \mathbf{X} + \mathbf{b}_1) + \mathbf{b}_2) \quad (1)$$

where \mathbf{X} is the input, \mathbf{Y} is the output; \mathbf{W}_1 and \mathbf{W}_2 are the convolutional weights for the first and second layers, respectively; \mathbf{b}_1 and \mathbf{b}_2 are the corresponding biases; and ReLU is the activation function. Despite leveraging the ReLU function, overly deep neural network architectures may still encounter vanishing or exploding gradients during the learning process, which limit the performance of a CNN (He et al., 2016; Alzubaidi et al., 2021). He et al. (2016) proposed ResBlocks to overcome this issue via shortcut. Equation (1) can be improved via shortcut as:

$$\mathbf{Y} = \text{ReLU}(F(\mathbf{X}) + \mathbf{X}) \quad (2)$$

where $F(\mathbf{X}) = \mathbf{W}_2 * \text{ReLU}(\mathbf{W}_1 * \mathbf{X} + \mathbf{b}_1) + \mathbf{b}_2$. He et al. (2016) constructed a CNN with 18 layers via ResBlocks (namely, ResNets 18) and obtained better performance than a traditional CNN model (i.e., VGG-16).

4.3. Lightweight attention module (LAM)

Traditional CNN models often process all evidence layers uniformly, without distinguishing their relative importances (Deng et al., 2022). However, individual evidence layers in most MPM carry varying weights (Porwal et al., 2003). AMs empower CNN models to identify and concentrate on the more critical parts of individual evidence layers, thereby improving the DL performance in MPM (Xu and Zuo, 2024). The CBAM is an integrated AM that consists of a channel AM and a spatial AM. The channel AM module highlights the importance of different channels, while the spatial AM module underscores the significance of various spatial locations. (Woo et al., 2018). The channel AM ($M_C(\mathbf{X})$) and the spatial AM ($M_S(\mathbf{X})$) are realized using operations such as convolution, pooling, and fully connected layers, as detailed respectively in the following equations:

$$M_C(\mathbf{X}) = \text{Sigmoid}(\text{MLP}(\text{AvgPool}(\mathbf{X})) + \text{MLP}(\text{MaxPool}(\mathbf{X}))) \quad (3)$$

$$M_S(\mathbf{X}) = \text{Sigmoid}(\text{Conv}_{7 \times 7}(\text{Concat}(\text{AvgPool}(\mathbf{X}), \text{MaxPool}(\mathbf{X})))) \quad (4)$$

where $\text{AvgPool}(\mathbf{X})$ refers to global average pooling, $\text{MaxPool}(\mathbf{X})$ represents global max pooling, $\text{MLP}(\cdot)$ refers to the multi-layer perceptron network, $\text{Concat}(\cdot)$ refers to concatenation of the results of max pooling and average pooling operations along the channel dimension, $\text{Conv}_{7 \times 7}(\cdot)$ refers to the convolution with a kernel size of 7×7 , and Sigmoid is the activation function (Woo et al., 2018).

The CBAM integrates a channel AM and a spatial AM respectively according to the following equations:

$$\mathbf{X}' = M_C(\mathbf{X}) \otimes \mathbf{X} \quad (5)$$

$$\mathbf{X}'' = M_S(\mathbf{X}') \otimes \mathbf{X}' \quad (6)$$

where \otimes denotes the element-wise product operation, \mathbf{X}' denotes the

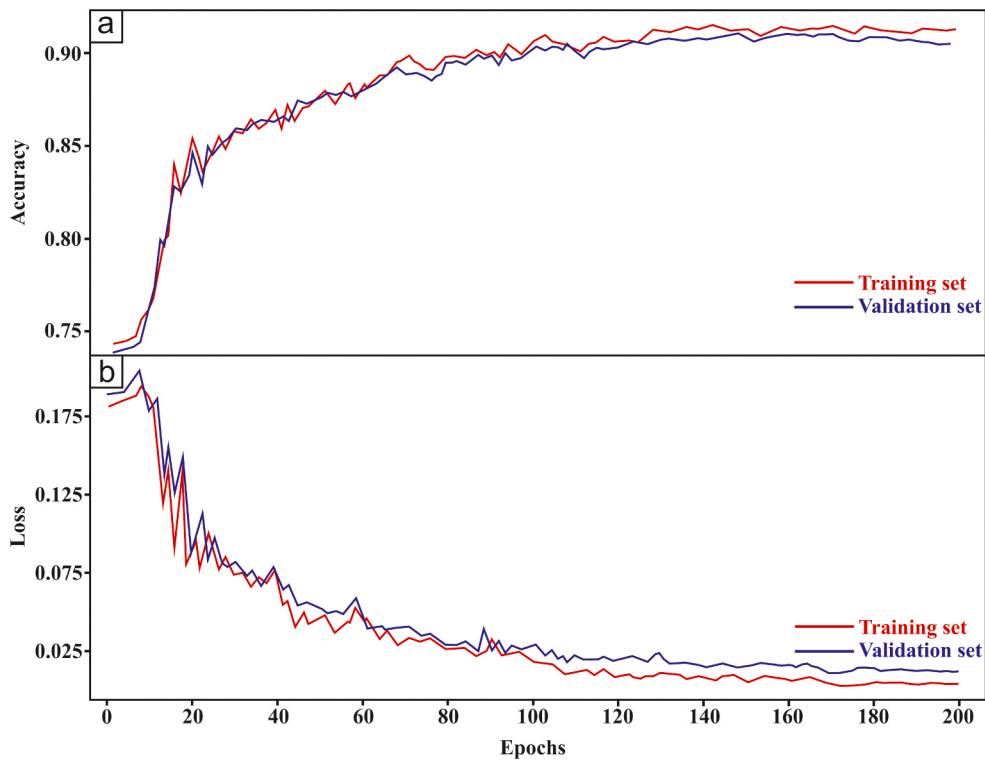


Fig. 9. (a) Accuracy (a) and (b) cross-entropy loss of DL4 model during training.

feature resulting from the channel AM, and \mathbf{X}'' denotes the final feature output by the CBAM. Liu et al. (2023) utilized a CBAM to improve the performance of a 2D CNN in 3D MPM. The above CBAM can be extended to 3D CNN with a large number of parameters. For instance, within the CBAM architecture, transitioning from a 2D 3×3 convolutional kernel to a 3D $3 \times 3 \times 3$ convolutional kernel results in a 3-fold increase in the number of parameters (Shi et al., 2021). Large-parameter DL models require more training samples and computational resources (Cui et al., 2021), which pose challenges and limit DL application to 3D MPM. Consequently, this study introduced the lightweight attention module (LAM), which consists of a lightweight channel AM ($M_{LC}(\mathbf{X})$) (Li et al., 2021b) and a spatial AM ($M_{LS}(X)$) (Shi et al., 2020) defined respectively as:

$$M_{LC}(\mathbf{X}) = \text{Sigmoid}(\text{FC}(\text{AvgPool}(\mathbf{X})) + \text{FC}(\text{MaxPool}(\mathbf{X}))) \quad (7)$$

$$M_{LS}(X) = \text{Sigmoid}(\text{Conv}_{DS}(\text{Concat}(\text{AvgPool}(X), \text{MaxPool}(X)))) \quad (8)$$

where $\text{FC}(\cdot)$ refers to the dimensionality reduction fully connected layer, and $\text{Conv}_{DS}(\cdot)$ refers to the depthwise separable convolution. Compared with $\text{MLP}(\cdot)$, the $\text{FC}(\cdot)$ decreases the number of channels, thus alleviating the complexity and computational burden of a DL model. The one-layer depthwise separable convolution consists of one-layer depthwise convolution ($\text{Conv}_{DW}(\cdot)$) and one-layer pointwise convolution ($\text{Conv}_{PW}(\cdot)$), which are defined respectively as:

$$\text{Conv}_{DW}(\mathbf{X}) = \mathbf{K}_{DW} * \mathbf{X} \quad (9)$$

$$\text{Conv}_{PW}(\mathbf{X}) = \mathbf{K}_{PW} * \text{Conv}_{DW}(\mathbf{X}) + \mathbf{b} \quad (10)$$

where \mathbf{K}_{DW} is the depthwise convolutional kernel, and \mathbf{K}_{PW} is the pointwise convolutional kernel. The depthwise separable convolution achieves the same functionality as standard convolution by initially applying depthwise convolution to process each channel independently, followed by combining the results through pointwise convolution. According to Eq. (1), the standard one-layer convolutional kernel can be represented as $\text{Conv}(\mathbf{X}) = \mathbf{W} * \mathbf{X} + \mathbf{b}$, and the number of parameters in \mathbf{W}

($N(\mathbf{W})$) can be calculated as:

$$N(\mathbf{W}) = C_{out} \times C_{in} \times D \times H \times W \quad (11)$$

where C_{in} and C_{out} denote the numbers of input and output channels, respectively; D , H and W represent the depth, height, and width of the convolutional kernel, respectively. The numbers of parameters in \mathbf{K}_{DW} ($N(\mathbf{K}_{DW})$) and \mathbf{K}_{PW} ($N(\mathbf{K}_{PW})$) can be calculated respectively as:

$$N(\mathbf{K}_{DW}) = C_{in} \times 1 \times H \times D \times W \quad (12)$$

$$N(\mathbf{K}_{PW}) = C_{out} \times C_{in} \times 1 \times 1 \times 1 \quad (13)$$

The total number of parameters in a one-layer depthwise separable convolution is $C_{in} \times H \times D \times W + C_{out} \times C_{in}$. Therefore, the depthwise separable convolution significantly reduces the number of parameters, especially when C_{out} is large, leading to even more substantial savings.

5. Results and discussion

5.1. DL dataset

This study developed a 3D residual CNN with LAM (RCNN-LAM) for 3D MPM. As a supervised DL model, the 3D CNN-LAM model requires datasets that consist of both positive and negative samples. This study produced 4101 positive samples with sizes of $3 \times 3 \times 3$ cells centered on known orebodies via sliding windows with one step size. The negative training samples for MPM should be distal from positive samples and distributed randomly spatially (Zuo, 2020). Following the criteria established by Zhang et al. (2019); Zhang et al. (2021), an equal number of negative samples, identical in cell size, were randomly generated in areas at least 800 m away from known orebodies (Fig. 8). The training samples were split into training and testing sets using a 7:3 ratio (Li et al., 2020b). Whereas the typical number of channels in image processing is three, corresponding to R (red), G (green) and B (blue), in this study, the positive and negative samples consist of seven channels, matching the number of evidence layers.

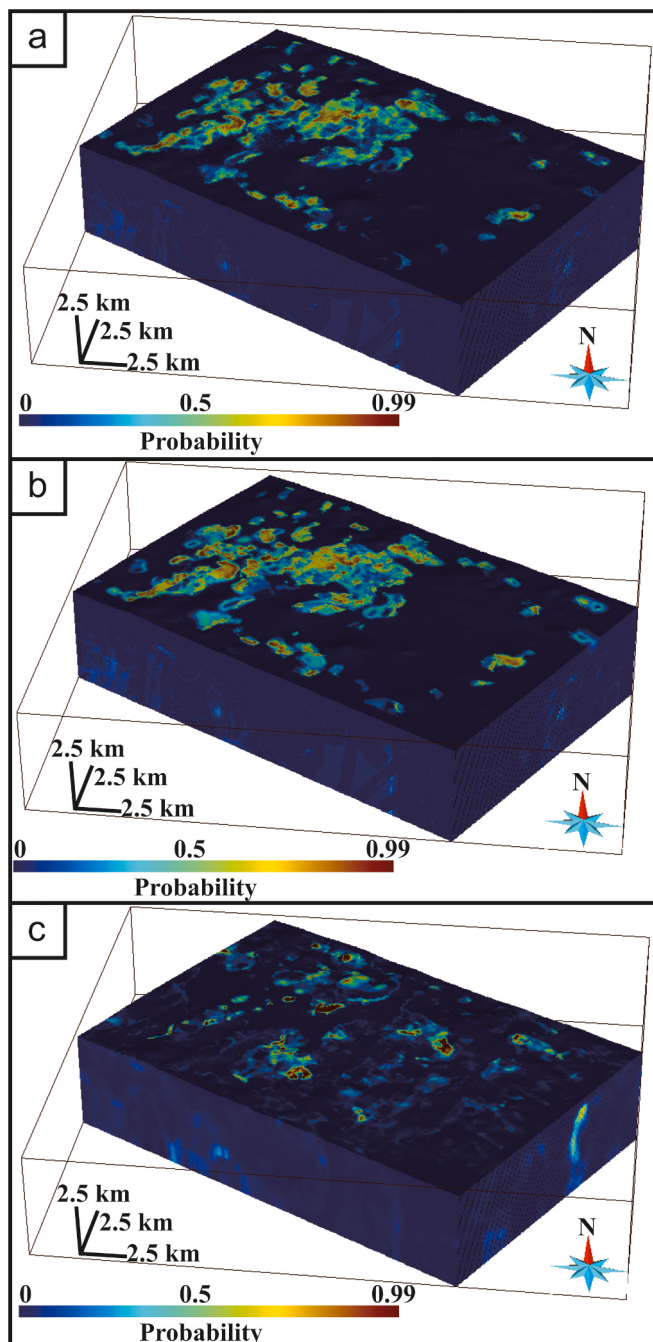


Fig. 10. 3D MPM results obtained by the (a) DL4, (b) DL2 and (b) RF models.

5.2. Comparative studies

The MPM model was trained on two NVIDIA A40 48 GB graphics cards. To identify the optimal configuration for the DL network, this study conducted an ablation experiment, which involved adding or removing a series of Resblock or Resblock with LAM (1–2) after one-layer convolution (Table 1). All neural network layers utilized the ReLu function as the activation function, except for the fully connected layer, which employed the Sigmoid function. The cross-entropy loss was utilized as the loss function. The ablation experiment indicated an optimal configuration (DL 4) for the DL network consisting of one-layer convolution, two-layer Resbolcks with LAM, and one-layer full connection (Tables 1 and 2, Fig. 2b). The optimal deep learning model was trained for 200 epochs using the Adam optimizer with a learning

rate of 0.001, resulting in stabilized accuracy and cross-entropy loss (Fig. 9). This study also compared the 3D MPM results of the DL modeling with RF modeling, which is widely used in MPM. The hyper-parameter tuning of the RF model was completed by the Bayesian optimization ($n_estimators = 77$, $max_depth = 7$, $max_features = 3$) (Zhang et al., 2022). The accuracy, AUC, and F1-score indicated that the DL model obtained better performance than the RF model (Table 1). Thus, the Resblock with LAM can improve the performance of DL modeling for 3D MPM. The 3D MPM results by the DL4, DL2, and RF are shown in Fig. 10. This study employed the widely used metrics of the number of parameters (NP) and floating-point operations (FLOPs) to evaluate the computational costs of the models (Table 1) (Shi et al., 2020; Li et al., 2021b; Zhang et al., 2023a). NP reflects the storage requirements and capacity of the model, while FLOPs quantify the number of mathematical operations required for a single forward pass. Typically, higher NP and FLOPs indicate increased model computational cost (Li et al., 2021b). Compared to the Resblock used in this study, the LAM achieves performance improvements without significant increases in NP and FLOPs, effectively balancing model performance and efficiency (Table 1).

5.3. 3D target delineation

The prediction—area (P—A) plot was employed to further compare the 3D MPM results obtained by DL4, DL2, and RF modeling (Fig. 11a, b, c) (Yousefi and Nykänen, 2016). The P—A plot was also utilized to delineate 3D targets in the study area (Fig. 11d, e, and f). The target areas identified by the RF model did not include the known SDG gold deposit (Fig. 11f). In contrast, the target areas identified by both the DL4 and DL2 models contained the known SDG gold deposit, highlighting the superiority of DL modeling (Fig. 11d and e). Also, the P—A plots demonstrate that the DL4 model achieved the best performance (Fig. 11a, b, and c). This indicates that the 3D LAM improves the performance of DL modeling for 3D MPM. Moreover, the target areas delineated by this study are concentrated mainly around the Early Cretaceous granodiorite model and the NE–NNE-striking fault model. For gold mineralization, the Early Cretaceous granodiorite supplied heat and ore-forming fluids whereas and the NE–NNE-striking faults provided pathways. Therefore, both the mathematical evaluations and geological interpretations confirm that using a 3D residual CNN combined with LAM is an effective method for 3D MPM.

6. Conclusions

DL algorithms, such as 3D CNN and AM, are adept at processing 3D voxel data, offering significant advantages for 3D MPM over traditional shallow ML methods. However, traditional 3D CNN and AM approaches require substantial computing resources. In response to this challenge, this study introduced a new approach that combines 3D residual CNN with LAM for 3D MPM. This approach has proven to be more effective than traditional 3D residual CNN and RF models in the Wulong gold district. Considering that exploration involves multiple stages, future studies may focus on integrating model-gradient adaptation and transfer learning-based model fine-tuning with the lightweight deep learning algorithm proposed in this study. This approach aims to achieve efficient 3D MPM throughout the entire exploration process, laying a foundation for subsurface exploration based on digital twin technology.

Declaration of competing interest

The authors declare that they have no known competing financial interests or personal relationships that could have appeared to influence the work reported in this paper.

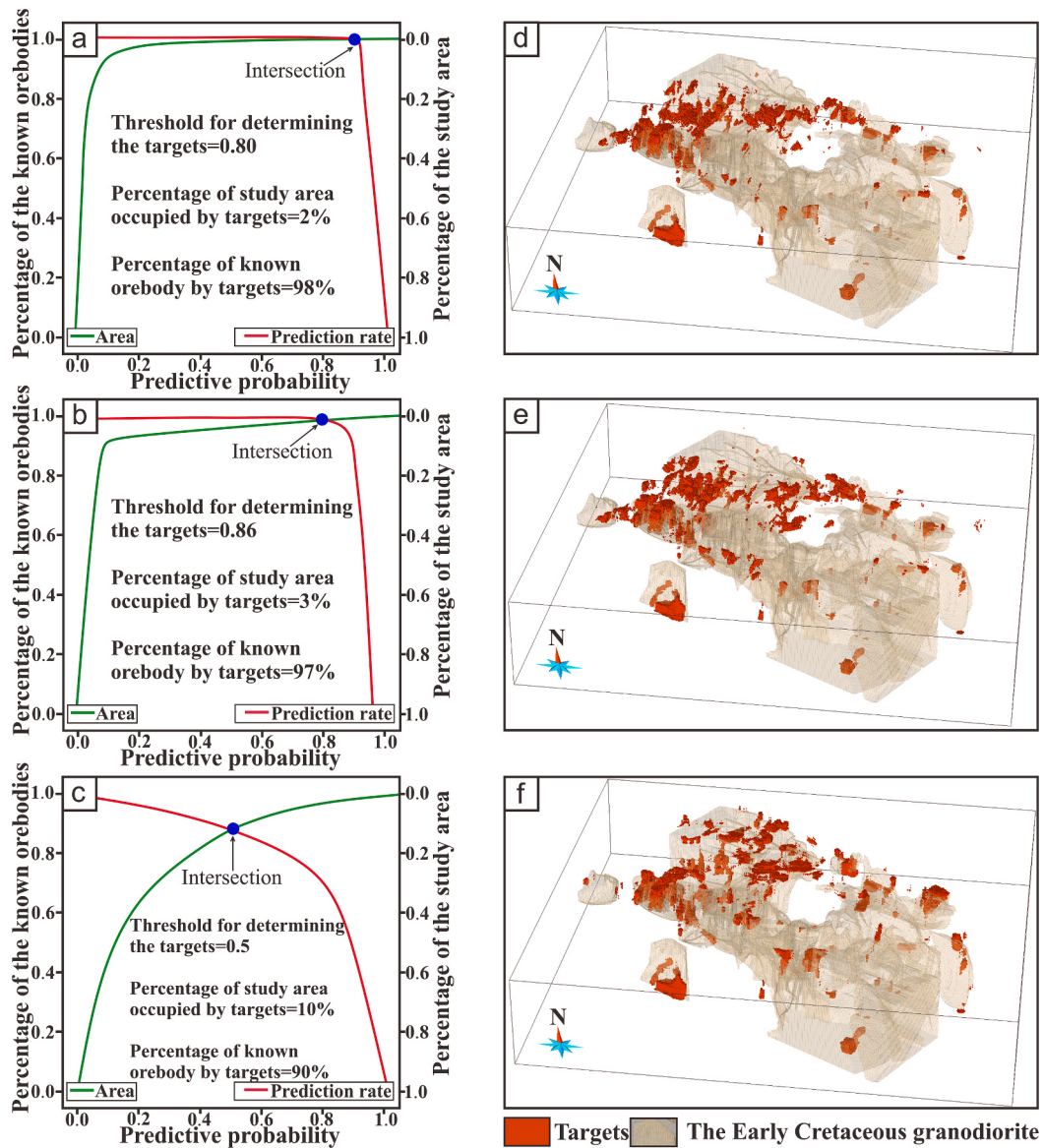


Fig. 11. P—A plots of the (a) DL4, (b) DL2, (b) RF models. 3D targets delineated by the (d) DL4, (e) DL, (f) RF models.

Acknowledgements

This study is joint funded by the National Science and Technology Major Project (Grant No. 2024ZD1001900), National Natural Science Foundation of China (Grant No. 42402301), Hebei Natural Science Foundations (Grant No. D2023403051 & D2024403084), National Key Research and Development Program of China (Grant No. 2022YFC2903600), MNR Key Laboratory for Exploration Theory & Technology of Critical Mineral Resources (Grant No. 202405), Yanzhao Golden Platform Talent Gathering Plan of Hebei Province (Grant No. B2025020), and Hebei GEO University PhD Research Start-up Fund Project (Grant No. BQ2024005). We would like to express our sincere gratitude to Managing Guest Editor Prof. Lingang Xu and two anonymous reviewers for their useful comments to improve this manuscript.

Data availability

The authors do not have permission to share data.

References

- Alzubaidi, L., Zhang, J., Humaidi, A.J., Al-Dujaili, A., Duan, Y., Al-Shamma, O., Santamaría, J., Fadhel, M.A., Al-Amidie, M., Farhan, L., 2021. Review of deep learning: concepts, CNN architectures, challenges, applications, future directions. *J. Big Data* 8, 1–74. <https://doi.org/10.1186/s40537-021-00444-8>.
- Carranza, E.J.M., Hale, M., Faassen, C., 2008. Selection of coherent deposit-type locations and their application in data-driven mineral prospectivity mapping. *Ore Geol. Rev.* 33, 3–4. <https://doi.org/10.1016/j.oregeorev.2007.07.001>.
- Chen, Y., 2015. Mineral potential mapping with a restricted Boltzmann machine. *Ore Geol. Rev.* 71, 749–760. <https://doi.org/10.1016/j.oregeorev.2014.08.012>.
- Cui, Y., An, Y., Sun, W., Hu, H., Song, X., 2021. Lightweight attention module for deep learning on classification and segmentation of 3-D point clouds. *IEEE Trans. Instrum. Meas.* 70, 1–12. <https://doi.org/10.1109/TIM.2020.3013081>.
- Deng, H., Zheng, Y., Chen, J., Yu, S., Xiao, K., Mao, X., 2022. Learning 3D mineral prospectivity from 3D geological models using convolutional neural networks: application to a structure-controlled hydrothermal gold deposit. *Comput. Geosci.* 161, 105074. <https://doi.org/10.1016/j.cageo.2022.105074>.
- Du, B., Wang, Z., Santosh, M., Shen, Y., Liu, S., Liu, J., Xu, K., Deng, J., 2023. Role of metasomatized mantle lithosphere in the formation of giant lode gold deposits: insights from sulfur isotope and geochemistry of sulfides. *Geosci. Front.* 14 (5), 101587. <https://doi.org/10.1016/j.gsf.2023.101587>.
- Feng, H., Shen, P., Zhu, R., Li, C., Ma, G., Pan, H., 2019. Geology and He-Ar-S-Pb isotope constraints on the genesis of the Sidaogou gold deposit in Liaodong Peninsula, northeastern North China Craton. *Ore Geol. Rev.* 113, 103080. <https://doi.org/10.1016/j.oregeorev.2019.103080>.

- Feng, H., Shen, P., Zhu, R., Tomkins, A.G., Brugger, J., Ma, G., Li, C., Wu, Y., 2023. Bi/Te control on gold mineralizing processes in the North China Craton: insights from the Wulong gold deposit. *Miner. Deposita* 58 (2), 263–286.
- Gholamalinezhad, H., and Khosravi, H. (2020). Pooling methods in deep neural networks, a review. arXiv preprint arXiv:2009.07485.
- Glorot, X., Bordes, A., and Bengio, Y. (2011, June). Deep sparse rectifier neural networks. In: Proceedings of the fourteenth international conference on artificial intelligence and statistics (pp. 315–323). JMLR Workshop and Conference Proceedings.
- Han, J., and Moraga, C. (1995, June). The influence of the sigmoid function parameters on the speed of backpropagation learning. In: International workshop on artificial neural networks (pp. 195–201). Berlin, Heidelberg: Springer Berlin Heidelberg.
- He, K., Zhang, X., Ren, S., Sun, J., 2016. Deep residual learning for image recognition. In: *Proceedings of the IEEE Conference on Computer Vision and Pattern Recognition*, pp. 770–778.
- Krizhevsky, A., Sutskever, I., Hinton, G.E., 2012. Imagenet classification with deep convolutional neural networks. In: *Advances in Neural Information Processing Systems*, p. 25.
- Li, J., Liu, X., Zhang, M., Wang, D., 2020a. Spatio-temporal deformable 3D Convnets with attention for action recognition. *Pattern Recogn.* 98, 107037.
- Li, S., Chen, J., Xiang, J., 2020b. Applications of deep convolutional neural networks in prospecting prediction based on two-dimensional geological big data. *Neural Comput. & Appl.* 32 (7), 2037–2053. <https://doi.org/10.1007/s00521-019-04341-3>.
- Li, T., Zuo, R., Xiong, Y., Peng, Y., 2021a. Random-drop data augmentation of deep convolutional neural network for mineral prospectivity mapping. *Nat. Resour. Res.* 30, 27–38. <https://doi.org/10.1007/s11053-020-09742-z>.
- Li, W., Li, J., Li, J., Huang, Z., Zhou, D., 2021b. A lightweight multi-scale channel attention network for image super-resolution. *Neurocomputing* 456, 327–337. <https://doi.org/10.1016/j.neucom.2021.05.090>.
- Li, X., Xue, C., Chen, Y., Yuan, F., Li, Y., Zheng, C., Zhang, M., Ge, C., Guo, D., Lan, X., Tang, M., Lu, S., 2023. 3D Convolutional Neural Network-based 3D mineral prospectivity modeling for targeting concealed mineralization within Chating area, middle-lower Yangtze River metallogenic Belt, China. *Ore Geol. Rev.*, 105444 <https://doi.org/10.1016/j.oregeorev.2023.105444>.
- Liu, Z., Yu, S., Deng, H., Jiang, G., Wang, R., Yang, X., Song, J., Chen, J., Mao, X., 2023. 3D mineral prospectivity modeling in the Sanshandao goldfield, China using the convolutional neural network with attention mechanism. *Ore Geology Reviews*, 105861.
- Lyu, M., Ren, B., Wu, B., Tong, D., Ge, S., Han, S., 2021. A parametric 3D geological modeling method considering stratigraphic interface topology optimization and coding expert knowledge. *Eng. Geol.* 293, 106300. <https://doi.org/10.1016/j.enggeo.2021.106300>.
- Manzi, M., Cooper, G., Malehmir, A., Durrheim, R., and Nkosi, Z. (2015). Integrated interpretation of 3D seismic data to enhance the detection of the gold-bearing reef: Mponeng Gold mine, Witwatersrand Basin (South Africa). *Geophysical Prospecting*, 63(4-Hard Rock Seismic imaging), 881–902. doi: 10.1111/1365-2478.12273.
- Olieroor, H.K., Scalzo, R., Kohn, D., Chandra, R., Farahbakhsh, E., Clark, C., Reddy, S.M., Müller, R.D., 2021. Bayesian geological and geophysical data fusion for the construction and uncertainty quantification of 3D geological models. *Geosci. Front.* 12 (1), 479–493. <https://doi.org/10.1016/j.gsf.2020.04.015>.
- Pang, Z., Wang, G., Qiu, H., Sun, S., Li, J., 2022. Geological and geochemical characteristics of the Wulong gold deposit, Liaodong Peninsula: Implications for gold mineralization. *Ore Geol. Rev.* 144, 104850. <https://doi.org/10.1016/j.oregeorev.vol.2022.104850>.
- Porwal, A., Carranza, E.J.M., Hale, M., 2003. Knowledge-driven and data-driven fuzzy models for predictive mineral potential mapping. *Nat. Resour. Res.* 12, 1–25. <https://doi.org/10.1023/A:1022693220894>.
- Ramachandran, P., Zoph, B., and Le, Q. V. (2017). Searching for activation functions. arXiv preprint arXiv:1710.05941.
- Rumelhart, D.E., Hinton, G.E., Williams, R.J., 1986. Learning representations by back-propagating errors. *Nature* 323 (6088), 533–536. <https://doi.org/10.1038/323533a0>.
- Shi, L., Xu, Y., Zuo, R., 2024. A heterogeneous graph construction method for mineral prospectivity mapping. *Nat. Resour. Res.* 1–12. <https://doi.org/10.1007/s11053-024-10344-2>.
- Shi, C., Zhang, X., Sun, J., Wang, L., 2021. A lightweight convolutional neural network based on group-wise hybrid attention for remote sensing scene classification. *Remote Sens. (Basel)* 14 (1), 161. <https://doi.org/10.3390/rs14010161>.
- Tao, J., Yuan, F., Zhang, N., Chang, J., 2021. Three-dimensional prospectivity modeling of Honghai volcanogenic massive sulfide Cu-Zn deposit, Eastern Tianshan, Northwestern China using weights of evidence and fuzzy logic. *Math. Geosci.* 53, 131–162. <https://doi.org/10.1007/s11004-019-09844-2>.
- Wang, G., Zhang, Z., Li, R., Li, J., Sha, D., Zeng, Q., Pang, Z., Li, D., Huang, L., 2021. Resource prediction and assessment based on 3D/4D big data modeling and deep integration in key ore districts of North China. *Sci. China Earth Sci.* 64, 1590–1606. <https://doi.org/10.1007/s11430-020-9791-4>.
- Wang, G., Zuo, R., 2022. Mineral prospectivity mapping using a joint singularity-based weighting method and long short-term memory network. *Comput. Geosci.* 158, 104974. <https://doi.org/10.1016/j.cageo.2021.104974>.
- Woo, S., Park, J., Lee, J.Y., Kweon, I.S., 2018. CBAM: Convolutional Block Attention Module. In: *Proceedings of the European Conference on Computer Vision (ECCV)*, pp. 3–19.
- Wu, X., Liu, G., Fan, W., Peng, S., Chen, G., Cheng, J., Wu, Y., 2024. Cross-sections compilation-adjustment method based on 2D-3D linkage in regional three dimensional geological modeling. *Earth Sci. Inf.* 17, 1067–1092. <https://doi.org/10.1007/s12145-024-01221-w>.
- Xiao, K., Xiang, J., Fan, M., Xu, Y., 2021. 3D mineral prospectivity mapping based on deep metallogenetic prediction theory: a case study of the LaLa Copper Mine, Sichuan, China. *J. Earth Sci.* 32 (2), 348–357. <https://doi.org/10.1007/s12583-021-1437-8>.
- Xiong, Y., Zuo, R., Carranza, E.J.M., 2018. Mapping mineral prospectivity through big data analytics and a deep learning algorithm. *Ore Geol. Rev.* 102, 811–817. <https://doi.org/10.1016/j.oregeorev.2018.10.006>.
- Xu, Y., Zuo, R., 2024. An interpretable graph attention network for mineral prospectivity mapping. *Math. Geosci.* 56, 169–190. <https://doi.org/10.1007/s11004-023-10076-8>.
- Yin, B., Zuo, R., Sun, S., 2023. Mineral prospectivity mapping using deep self-attention model. *Nat. Resour. Res.* 32, 37–56. <https://doi.org/10.1007/s11053-022-10142-8>.
- Yin, B., Zuo, R., Xiong, Y., 2022. Mineral prospectivity mapping via gated recurrent unit model. *Nat. Resour. Res.* 31, 2065–2079. <https://doi.org/10.1007/s11053-021-09979-2>.
- Yousefi, M., Nykänen, V., 2016. Data-driven logistic-based weighting of geochemical and geological evidence layers in mineral prospectivity mapping. *J. Geochem. Explor.* 164, 94–106. <https://doi.org/10.1016/j.gexplo.2015.10.008>.
- Yu, B., Zeng, Q., Frimmel, H.E., Wang, Y., Guo, W., Sun, G., Zhou, T., Li, J., 2018. Genesis of the Wulong gold deposit, northeastern North China Craton: constraints from fluid inclusions, H-O-S-Pb isotopes, and pyrite trace element concentrations. *Ore Geol. Rev.* 102, 313–337. <https://doi.org/10.1016/j.oregeorev.2018.09.016>.
- Zhang, B., Xu, K., Khan, U., Li, X., Du, L., Xu, Z., 2023a. A lightweight convolutional neural network with end-to-end learning for three-dimensional mineral prospectivity modeling: a case study of the Sanhetun Area, Heilongjiang Province, Northeastern China. *Ore Geol. Rev.*, 105788 <https://doi.org/10.1016/j.oregeorev.2023.105788>.
- Zhang, Z., Wang, G., Carranza, E.J.M., Liu, C., Li, J., Fu, C., Liu, X., Chen, C., Fan, J., Dong, Y., 2023b. An integrated machine learning architecture with uncertainty quantification for three-dimensional lithological modeling from multi-source geophysical data and drilling data. *Eng. Geol.* 324, 107255. <https://doi.org/10.1016/j.jeng.geo.2023.107255>.
- Zhang, Z., Wang, G., Carranza, E.J.M., Zhang, J., Tao, G., Zeng, Q., Sha, D., Li, D., Shen, J., Pang, Z., 2019. Metallogenetic model of the Wulong gold district, China, and associated assessment of exploration criteria based on multi-scale geoscience datasets. *Ore Geol. Rev.* 114, 103138. <https://doi.org/10.1016/j.oregeorev.2019.103138>.
- Zhang, Z., Wang, G., Carranza, E.J.M., Fan, J., Liu, X., Zhang, X., Dong, Y., Chang, X., Sha, D., 2022. An integrated architecture for data-driven mineral prospectivity mapping using bagging-based positive-unlabeled learning and bayesian cost-sensitive logistic regression. *Nat. Resour. Res.* 31, 3041–3060. <https://doi.org/10.1007/s11053-022-10120-0>.
- Zheng, F., Xu, T., Ai, Y., Yang, Y., Zeng, Q., Yu, B., Zhang, W., Xie, T., 2022. Metallogenetic potential of the Wulong goldfield, Liaodong Peninsula, China revealed by high-resolution ambient noise tomography. *Ore Geol. Rev.* 142, 104704. <https://doi.org/10.1016/j.oregeorev.2022.104704>.
- Zhu, R., Yang, J., Wang, G., Zeng, Q., Xue, G., Xu, T., Li, X., Zhang, P., Lei, D., Zhu, G., 2024. The genesis and resource potential of gold deposits in the Liaodong Peninsula. *Sci. China Earth Sci.* 67, 657–672. <https://doi.org/10.1007/s11430-023-1258-4>.
- Zuo, R., 2020. Geodata science-based mineral prospectivity mapping: a review. *Nat. Resour. Res.* 29, 3415–3424. <https://doi.org/10.1007/s11053-020-09700-9>.
- Zuo, R., Carranza, E.J.M., 2011. Support vector machine: a tool for mapping mineral prospectivity. *Comput. Geosci.* 37 (12), 1967–1975. <https://doi.org/10.1016/j.cageo.2010.09.014>.